

# Fluorescence Tracking and $\mu$ -PIV of Individual Particles and Lubricant Flow in and Around Lubricated Point Contacts

V. Strubel<sup>1</sup> · S. Simoens<sup>2</sup> · P. Vergne<sup>1</sup> · N. Fillot<sup>1</sup> · F. Ville<sup>1</sup> · M. El Hajem<sup>2</sup> · N. Devaux<sup>1</sup> · A. Mondelin<sup>3</sup> · Y. Maheo<sup>3</sup>

Received: 24 January 2017 / Accepted: 24 April 2017 / Published online: 4 May 2017  
© Springer Science+Business Media New York 2017

**Abstract** This paper deals with optical experimental methods for improving current knowledge on particle entrapment in elastohydrodynamic contacts. Particular attention was paid to the possibilities offered by fluorescence-based techniques for mapping lubricant flow and tracking contaminant trajectories. A ball-on-disk tribometer, a fluorescent medium, and particle image velocimetry equipment were used together for this purpose. This original experimental setup enabled us to obtain lubricant streamlines and velocity vector maps in the contact area. Moreover, it allowed us, for the first time, to capture the details of trapping as the rejection of contaminating particles, in the context of lubrication, as it happened. Dynamic in situ observations clearly showed that the entrapment of debris-like particles was competing against the backflow occurring upstream, in particular in elliptical contacts. The results reported in this work confirm and expand previous results obtained with different methods, i.e., using a twin-disk machine and CFD computations. Finally, we briefly describe as future work the potential for applying these fluorescence-based methods to questions that are still under debate in the lubrication community.

**Keywords** Particle entrapment · Particle tracking · Particle image velocimetry · Fluorescence · Point contacts · Elliptical contacts

## List of symbols

$a$	Hertzian radius or ellipse semi-axis in the $x$ -direction ( $\mu\text{m}$ )
$b$	Ellipse semi-axis in the $y$ -direction ( $\mu\text{m}$ )
$k = b/a$	Ellipticity ratio (–)
$N_{\text{pix},x}$	Number of pixels of the camera sensor along the $x$ -direction (–)
$N_{\text{pix},y}$	Number of pixels of the camera sensor along the $y$ -direction (–)
$P_H$	Hertzian pressure (MPa)
$R_x$	Ball radius or radius of curvature in the $x$ -direction (mm)
$R_y$	Radius of curvature in the $y$ -direction (mm)
$t$	Time (s)
$T_s$	Sequential lighting time (s)
$U_m$	Mean entrainment speed (m/s) = $(U_1 + U_2)/2$
$U_1$	Velocity of the disk at the contact location in the $x$ -direction (m/s)
$U_2$	Velocity of the metallic sample (ball- or barrel-shaped) at the contact location in the $x$ -direction (m/s)
$w$	Normal load (N)
$\Delta t$	Synchronized separation time (s)
$\Delta t_x$	Synchronized separation time defined in the $x$ -direction (s)
$\Delta t_y$	Synchronized separation time defined in the $y$ -direction (s)
$\Delta X$	Size of the camera image in $x$ -direction (m)

✉ N. Fillot  
nicolas.fillot@insa-lyon.fr

P. Vergne  
philippe.vergne@insa-lyon.fr

<sup>1</sup> Univ Lyon, INSA Lyon, CNRS, LaMCoS UMR5259, 69621 Villeurbanne, France

<sup>2</sup> Univ Lyon, EC Lyon, CNRS, LMFA UMR5509, 69134 Écully, France

<sup>3</sup> SKF Aerospace, 26300 Châteauneuf-sur-Isère, France

## 1 Introduction

After decades of thorough analyses to obtain film thickness, temperature, pressure, and shear rate distributions in the Hertzian pressurized area in elastohydrodynamic (EHD) contacts, as recently reviewed by Albahrani et al. [1], research in lubrication is paying more attention to understanding phenomena occurring around and, in particular, upstream of this area. This region is indeed relevant for the study of issues such as the contact-feeding regime (fully flooded or starved), the onset of shear-heating or shear-thinning effects, or contaminating particle entrapment, which are all important concerns.

Nowadays, particle image velocimetry (PIV), often based on the detection of the motion of fluorescent dyes, is becoming a key technique for the measurement and control of flows at different scales and in diverse applications [2–4]. Faster applications, smaller channels (micro-PIV or  $\mu$ -PIV), and nonconventional fluids have caused this technique to evolve and become suitable for a very broad range of fluid mechanics applications. By combining buoyant fluorescent particles, an adapted lighting source, and suitable recording and analyzing facilities, it has become possible to determine the motion of particulate tracers and thus to capture flow details within lubricated contacts and in their vicinity.

Previous tribological studies have already used fluorescence or PIV in diverse flow configurations. Using an incandescent source and glass particles, Bair et al. [5] determined in 1993 the mechanisms leading to the limiting shear stress phenomenon, by observation of the motion of glass spheres within a high-pressure cell. With the development of epifluorescent microscopy and related techniques, fluorescent dye particles have been employed in more recent works to investigate lubricated contact features. Reddyhoff and coworkers [6] used in 2010 a method that was similar to but much improved over that used by Bair et al. to monitor the lubricant flow in a contact formed between a steel ball and a glass disk, using a fluorescent dye deposited upstream. With a dedicated PIV optical setup, Horvat and Braun [7] were able to capture the flows occurring in the pockets of a hydrostatic journal bearing in which dye particles were tracked in a Lagrangian fashion, enabling them to determine the instantaneous velocity vector fields. Li et al. [8] applied the  $\mu$ -PIV technique to follow the grease motion in narrow channels with different restrictions: They showed that in some cases a large amount of the grease was not moving. Ponjavic et al. [9] used another fluorescence-based technique (fluorescence recovery after photobleaching, FRAP) to analyze through-thickness velocity profiles and establish whether or not homogenous shear could occur, according to the operating

conditions. Finally, in 2016, Albahrani and coworkers [10] utilized the photoluminescence properties of quantum dots to map pressure and temperature within EHD contacts. Therefore, the application of fluid mechanics techniques to lubrication has provided experimental evidence—or confirmations of previous numerical findings—on fluid behavior in lubricated contacts. Moreover, this approach can enable direct observation of contaminating particles (e.g., fluorescent dyes) that might be carried within EHD contacts.

In the present work, fluorescence-based measurements and  $\mu$ -PIV analyses were conducted with the aim of highlighting particular features of lubricated contacts and of emphasizing the key role of some lubricant flows in leading to or competing against particle entrapment. First, the methodology used to track the steel contaminants to be entrapped is presented. It is then shown that a  $\mu$ -PIV analysis of the contact inlet enables us to determine the distribution of instantaneous velocity vectors in that region. The technique was applied to prove experimentally the importance of backflows occurring in lubricated contacts for the particle entrapment phenomenon. Finally, some perspectives on new research utilizing these techniques are proposed.

Note that in this work, the size of the contaminating particles considered was always larger than the contact film thickness (as it can be estimated from semi-analytical EHD expressions). Therefore, entrapment was expected to occur—when possible—in a region located upstream of the area of classical Hertzian pressure. Thus, the terms “contact” or “contact area” should be understood here in a broad sense that includes, for example, the inlet and/or the exit zone.

## 2 Experimental Tools

The test rig used in this work was a ball-on-disk tribometer developed in-house [11] (Fig. 1), designed for simulating EHD contacts over a large range of rolling/sliding speeds, with various materials (steel, glass, sapphire, carbide, etc.) and geometrical configurations (circular or elliptical). In this work, it was operated under pure rolling and fully flooded conditions. The metallic samples used in this work were machined from AISI 52,100 bearing steel, and the disks were made from Pyrex glass. The materials' properties are given in Table 1, and the different geometries are presented in Table 2, where  $R_x$  and  $R_y$  are the radii along the rolling and transverse directions, respectively. These different configurations lead to point contacts of different ellipticity ratios,  $k = b/a$  (where  $b$  and  $a$  are the ellipse semi-axes in the  $x$ - and  $y$ -directions): 1.0, 3.46, and 8.02.

**Fig. 1** Schematic of the ball-on-disk tribometer with the  $\mu$ -PIV system

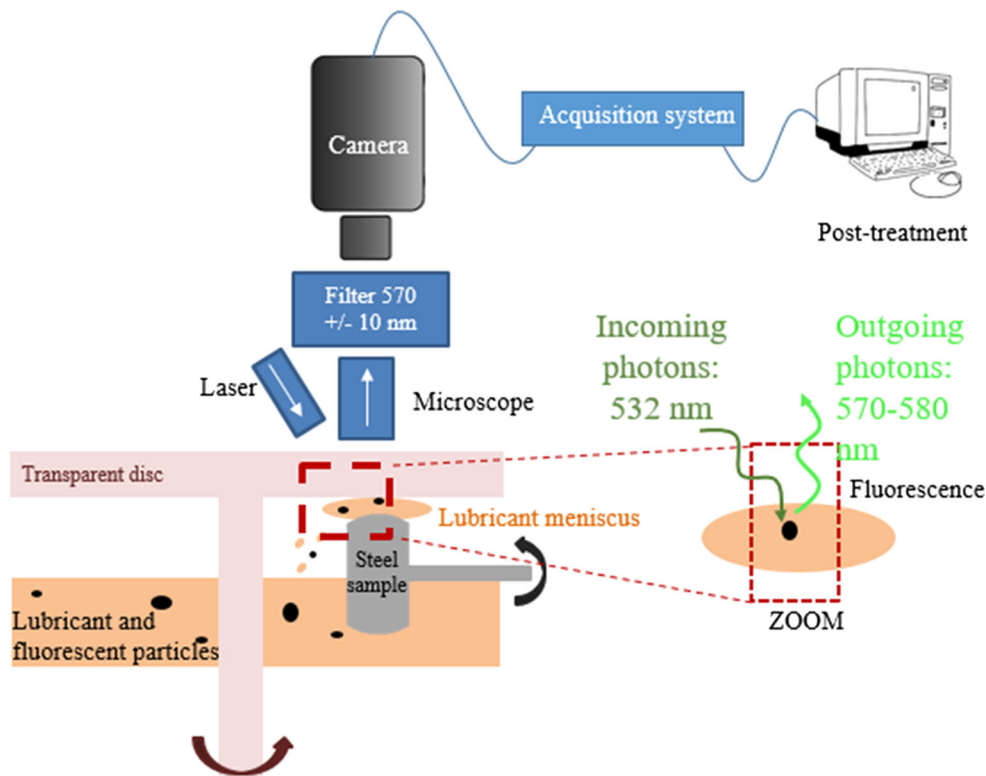


**Table 1** Material properties of the specimen

	AISI 52100	Pyrex
Young's modulus (GPa)	210	64
Poisson ratio	0.3	0.2
Hardness	HRC 64	Knoop hardness (kg/mm <sup>2</sup> ) 418
Density (kg/m <sup>3</sup> )	7800	2230

**Table 2** Parameters defining the contact between a Pyrex disk and a steel ball (or barrel) for circular (or elliptical) contacts

	Circular case	Elliptical contacts	
$R_x$ (mm)	12.7	13.1	13
$R_y$ (mm)	12.7	84.2	330
$W$ (N)	10	50	50
$P_H$ (MPa)	312	307	226
$a$ ( $\mu$ m)	124	151	115
$b$ ( $\mu$ m)	124	513	920
$k = b/a(-)$	1.00	3.46	8.02

By using an adequate combination of buoyant particles, a lighting source, and a recording and analyzing device, it is possible to track the motion of particle tracers and thus determine the characteristics of any type of flow. Fluorescent particles were chosen as fluid tracers in this study. They were part of a commercially available paint provided

by Lefranc et Bourgeois<sup>®</sup>: the red fire fluorescent paint in which the particles of interest are made of rhodamine pigments embedded in a melamine–formaldehyde–sulfonamide copolymer. Rhodamine is known to react inelastically to light excitation: From a wavelength of 532 nm, an induced fluorescent emission is recorded at around 570 nm [4, 12]. The particle size distribution of the tracers shows the major size class of fluorescent particles to be  $10 \pm 4 \mu\text{m}$  (Fig. 2). The lubricant used during the tests was composed of 25 ml of a commercial turbine oil to which a mixture of 1 g of paint and 1 ml of ethanol were previously added, in order to ensure a homogeneous seeding. The turbine oil had a density of  $875 \text{ kg/m}^3$  at  $20^\circ\text{C}$ , and that of the paint was  $1080 \text{ kg/m}^3$  at ambient temperature. The proportions of this mixture were chosen according to the requirements imposed by both the visualization method and the very small volumes under consideration. A rough estimation led to about 3–4000 dye particles/mm<sup>3</sup>, resulting in a volume fraction lower than 0.2%. Therefore, the addition of the dye particles may have

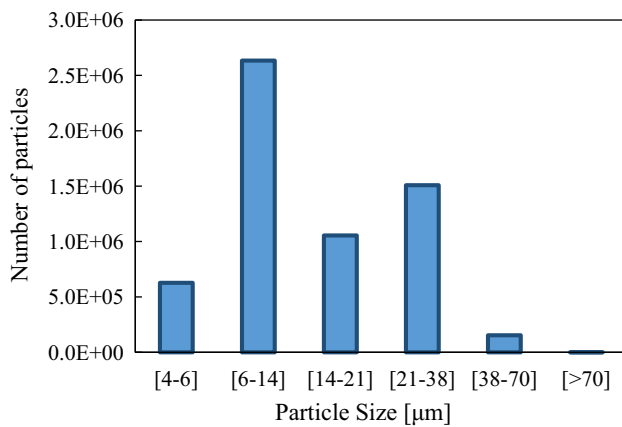


**Fig. 2** Size distribution of the rhodamine tracers in the red fire fluorescent paint provided by Lefranc et Bourgeois®

a weak influence on the lubricant viscosity, but this can, in no way, alter the flow nature and its distribution upstream and around the contact spot.

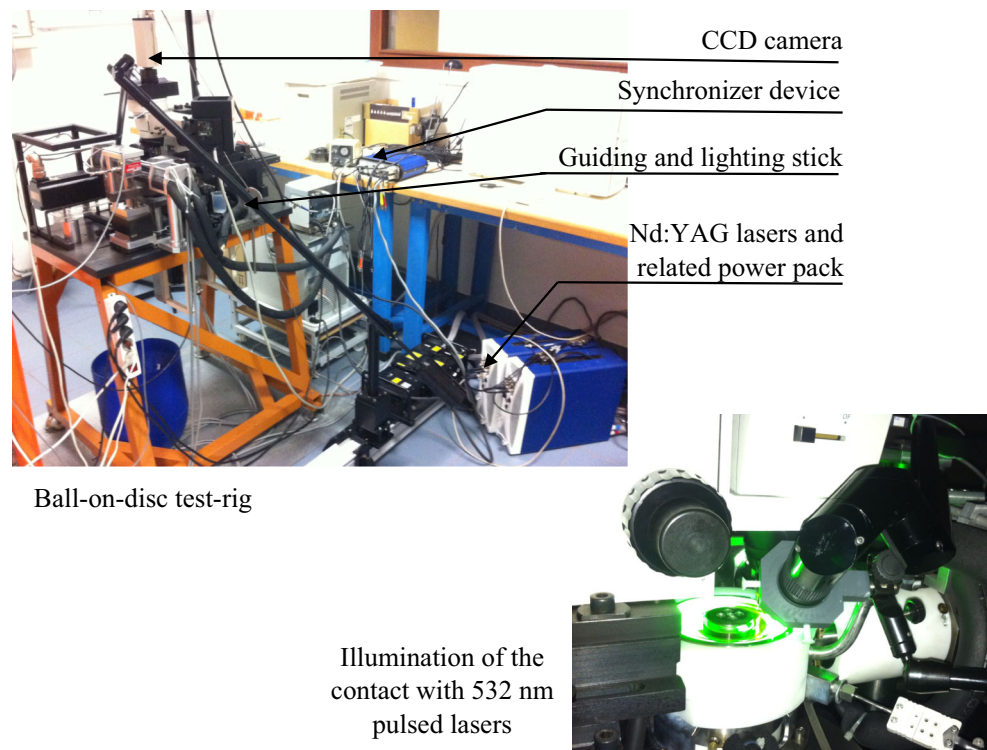
The light source consisted of two synchronized Nd:YAG pulsed lasers (532 nm, 150 mJ); the planar beams were guided toward the test rig through a guiding and lighting device, composed of mirrors and optical tubes (Fig. 3). A CCD camera (Kodak Megaplus ES 1.0) with a  $1008 \times 1018$  pixels sensor was used to record digital frames, and a dedicated software (DaVis from LaVision) was used to analyze the particle trajectories. A band-pass filter FB-570-10 (570 nm, with full width at half maximum

(FWHM) of 10 nm) was inserted in the optical path between the illuminated zone and the camera to capture the fluorescence signal only and reject the incident source, as well as all other parasitic lights.

The coupling of two pulsed laser sources provides different possibilities for visualizing the lubricant's flow. The two pulsed lasers could sequentially stimulate the fluorescent particles as follows. The synchronized separation time  $\tau$  (the delay between two laser pulses from laser A and laser B; see Fig. 4) and the sequential lighting time  $T_s$  (the time between two consecutive series of laser pulses; also shown in Fig. 4) were set to synchronize the laser beams at two different frequencies: a rather low frequency ( $= 1/T_s$ ), imposed by the technical capability of the lasers (the charging time in this case, limited to a minimum of ca. 66 ms), and a much higher frequency ( $= 1/\Delta t$ ) driven by the synchronizing device only. The recording of the CCD camera frames was also synchronized with the two lasers.

For a given  $T_s$ , the transient observation of the particles motion, also called particle tracking, could be performed thanks to the sequential laser shots. Indeed, the latter enables us to obtain particle trajectories by tracking the particles' positions as long as they remain in the camera's field of view, and if  $T_s$  is low enough compared with the particles' transit time. The synchronized separation time between the two laser pulses—in a range varying from a few microseconds to a few milliseconds—allowed us to determine the fluid velocity field by the classical PIV

**Fig. 3** Ball-on-disk test rig coupled with the PIV system composed of an illumination source/guiding and lighting device/CCD camera/synchronizer device



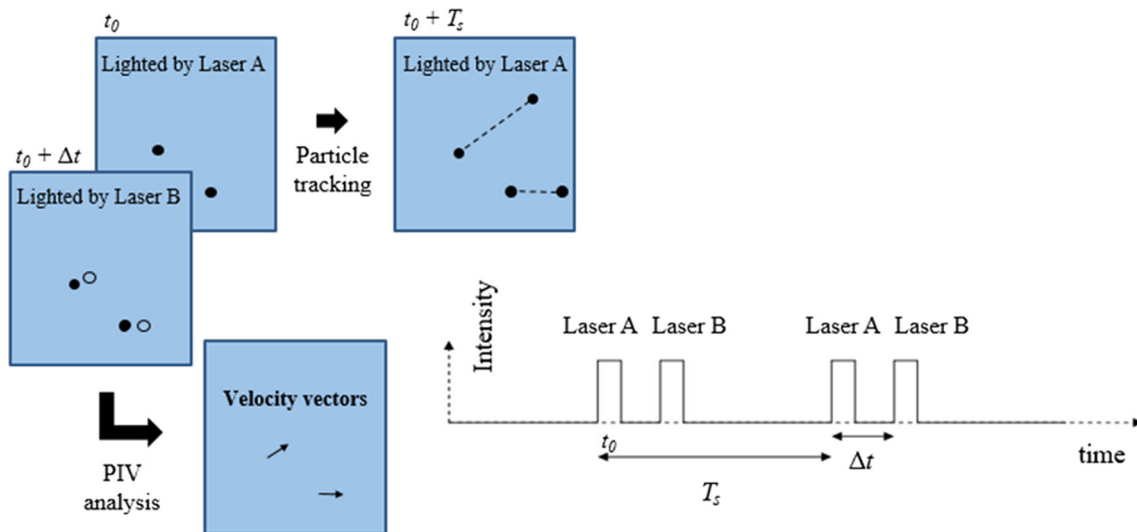


**Fig. 4** Principle of synchronized pulsed lasers to perform particle tracking and particle image velocimetry (PIV)

method, in which a suitable value of  $t$  gives two consecutive and close positions of the seeding particles. The camera was able to capture images, in two separate frames taken at two successive instants, of the same set of fluorescent particles located in its field of view.

A cross-correlation algorithm was used on the subdivided sections, or meshes, of the recorded frames and enabled us to determine the displacement of the particles and the corresponding instantaneous velocity vectors. The  $\mu$ -PIV measurements require the recording of a small displacement, which in our case was a function of the mean entrainment speed, and the mesh size ( $N_{\text{pix},x} \times N_{\text{pix},y}$ ) gave the spatial resolution of the technique out of the laser beam dimension. A microscope with a  $\times 10$  magnification objective was used in the present study, leading to a spatial resolution of  $1.8 \mu\text{m}/\text{pixel}$  and a depth of focus of  $15 \mu\text{m}$ . A displacement of about ten pixels or more (for an analysis mesh size of 32 pixels) was imposed to ensure that around two-thirds of the particles of the set would be present in the two frames and a same mesh [13], so that the synchronized separation time can be defined by

$$\Delta t_x \geq \frac{10 \frac{\Delta X}{N_{\text{pix},x}}}{U_m} \tag{1}$$

where  $\Delta X$  is the size of the CCD sensor of the camera in the  $x$ -direction,  $N_{\text{pix},x}$  is the number of pixels along the  $x$ -direction, and  $U_m$  is the mean entrainment speed.

The same constraint is applied to the  $y$ -direction and  $\Delta t = \min(\Delta t_x, \Delta t_y)$ . Table 3 presents the relationship between the imposed entrainment velocity (varying from 0.005 to 3 m/s) and  $t$  to perform a relevant  $\mu$ -PIV analysis. The latter parameter corresponds to the required delay between lasers A and B to successively lighten the

**Table 3** Correspondence between the mean entrainment speed and the synchronized separation time (delay between the pulses of the two lasers) for  $\mu$ -PIV analysis

$U_m$ (m/s)	0.005	0.01	0.02	0.04	0.1	0.2	1.5	3
$\Delta t$ ( $\mu\text{s}$ )	10,000	5000	2000	1000	500	200	20	10

lubricant flow and allows the mapping of the instantaneous velocity vectors.

Therefore, the PIV technique can provide two different types of results: either by tracking particles' trajectories in a Lagrangian-type description, or by observing particles that pass through a fixed stationary area in a Eulerian fashion. The first type needs either very close pulses delivered by two distinct lasers or a rather slow particle speed, whereas the second approach depends only on the delay between two successive lighting pulses produced from the same laser or two synchronized lasers. The techniques applied here are inspired from those presented by Santiago et al. [3] to which the reader can refer for more details. Also, references [14, 15] provide a more general insight into the PIV method.

### 3 Results and Discussion

#### 3.1 Lubricant Velocity Distribution Around an EHD Contact

By combining the fluorescence technique with  $\mu$ -PIV analysis, it was possible to map the velocity vectors of the lubricant moving around a circular EHD contact. The lubricant was seeded with rhodamine particles to allow

mapping of the fluid flow. As the contacts remain stationary in time and position, the periodic lighting with two different lasers (Fig. 4) enabled us to follow the small displacements of the tracers. Thus, assuming that the fluid follows the same trajectories as the dye particles over small-amplitude displacements, velocity vectors between successive nearby positions could be determined by choosing an adequate synchronized sequential separation time between the two lasers (see Table 3). The mapping of the velocity vectors was obtained by a  $\mu$ -PIV analysis performed on successive frame pairs (related to the synchronized light pulses sent by lasers A and B) as recorded by the camera. Typically, 100 deduced velocity fields found from 100 frame pairs were averaged. This procedure enabled us to obtain a unique map of the mean velocity vectors of the lubricant in the inlet zone. Moreover, it should be noted that the separation time depends only on the flow regime and the value of the sequential lighting time is not accounted for. As a consequence, in the case of a stationary flow, the mean entrainment speed accessible by this method ranged from 0.005 to 3 m/s. Figures 5 and 6 show the instantaneous velocity distributions obtained for the entrainment speeds of 0.005 and 0.5 m/s, respectively. The Hertzian contact area is represented by a striped disk, and the length of the white arrows represents the magnitude of the velocity vectors. A black zone just around the contact is excluded from the representation as too few particles enter this domain, resulting in insufficient information for a proper PIV analysis. The orientation and length of the white arrows indicate that a large amount of lubricant is bypassing the contact. The lubricant slows down upstream of the Hertzian zone along the central contact axis in both figures, but it accelerates everywhere else. Also, only a very low proportion of lubricant is carried toward the Hertzian contact area in both figures. At 0.005 m/s (Fig. 5), the map is more scattered than the one at 0.5 m/s (Fig. 6), especially on the contact sides (corresponding to the right-upper and right-lower parts of the figures), as fewer rhodamine particles are dragged toward the contact area at low entrainment velocity. This trend is consistent with the work of Hsiao et al. [16], who proposed a numerical evaluation of the lubricant flow in EHD contacts through streamlines analysis. They found the presence of strong side-flows leading to about 5% only of the lubricant being present upstream to reach the Hertzian contact zone.

Experimentally mapping the velocity vectors offers new opportunities to validate some of the many numerical models published in the literature. Indeed, numerical solutions rely on boundary conditions that are difficult to define and model in the vicinity of EHD contacts (see, for example, the work of Bruyere [17], dealing with a two-phase flow model of the contact outlet). Here, a comparison was performed between experimental results (from

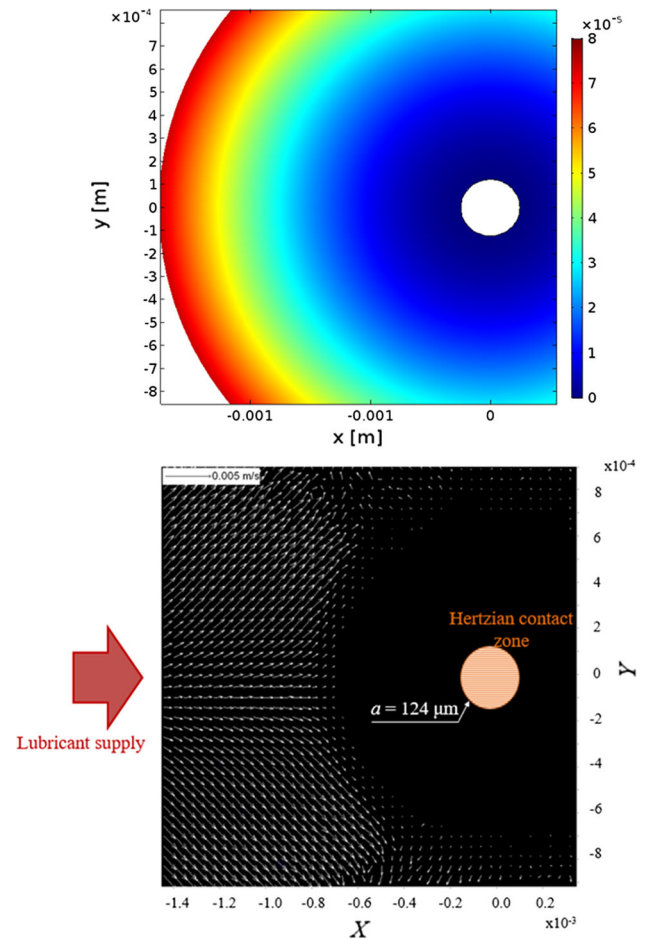


**Fig. 5** Mapping of the instantaneous velocities (*bottom figure*) from a  $\mu$ -PIV analysis of the inlet zone of a circular steel–glass contact. The *top figure* shows the gap thickness. Operating conditions:  $U_m = 0.005$  m/s,  $w = 10$  N

$\mu$ -PIV experiments) and numerical ones obtained with the model presented in [18] based on a Multiphysics finite elements method (FEM) solver described in [19, 20]. Figure 7 shows the superposition of velocity vector distributions obtained experimentally and numerically for a glass–steel contact, a mean entrainment speed of 0.5 m/s, and a normal load of 10 N. It is important to notice that this comparison was realized with (1) numerical mapping of the fluid velocity vectors obtained over a median height (Fig. 7, right) and (2) experimental mapping of the fluid velocity vectors averaged over the depth of focus given by the objective of the microscope (Fig. 7, left). In the experiments, the microscope adjustment was made in such a way to focus on the median plane in between the two moving solid surfaces, as indicated for the numerical simulations in the top-right schematic in Fig. 7. This made it possible to compare the two approaches carried out under fairly similar conditions. Few discrepancies appear between the two distributions. The more visible

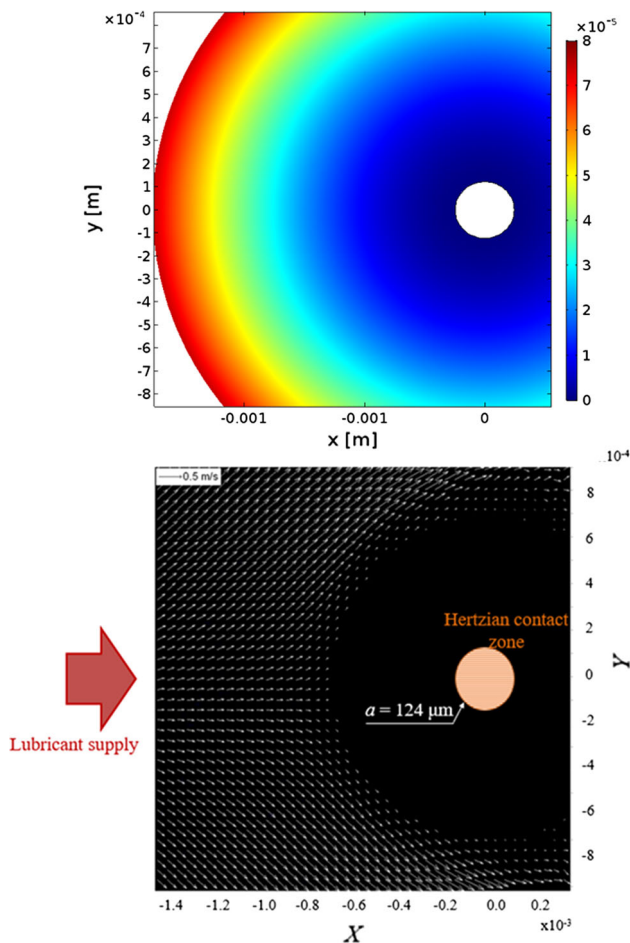


**Fig. 6** Mapping of the instantaneous velocities (bottom figure) from a  $\mu$ -PIV analysis of the inlet zone of a circular steel–glass contact. The top figure shows the gap thickness. Operating conditions:  $U_m = 0.5$  m/s,  $w = 10$  N

deviations were located near the left-lower edge, which represents the part of the domain with the thickest lubricant film. This gap could be reduced by using an objective with a much smaller depth of field to capture only velocity values over a very thin slab of fluid.

It might be surprising to observe that, along the central axis (i.e., for  $y = 0$ ), the velocity vectors corresponded to much lower values than the main applied entrainment speed  $U_m$  of 0.005 or 0.5 m/s (Figs. 6, 7). In fact, the velocity distributions presented in Figs. 5, 6, and 7 represent the lubricant flow at an intermediate thickness and not in the vicinity of the walls, which themselves move at a speed equal to  $U_m$ . Furthermore, the gap restriction caused by the presence of the contact (and of the ball in this case) leads to a very variable velocity profile across the thickness of the film upstream of the contact, and this can evolve as far as a reversal of the flow direction at some locations.

### 3.2 Entrapment of Debris-Like Particles

The entrapment of contaminating particles is a tribological phenomenon that is difficult to capture experimentally as it occurs on the micrometric scale and within a short time-frame. Several attempts have been made to observe particle entrapment using the interferometric technique and a ball-on-disk machine [21, 22]. Cann et al. [21] used a conventional interferometric setup with a silica coating on a transparent disk. The presence of a trapped particle within the contact area was determined only after the particle had escaped from the place of entrapment, i.e., the interface between the entrapped particle and the disk. The entrapment mark was indicated afterward by an uncolored interference fringe. With this method, particle trapping could be observed in the Hertzian contact zone only. Thus, a strong limitation on particle size (submicrometric) was imposed, because with the interferometric technique, film thickness is known to be measurable in the typical range of 0–800 nm [11]. In the present study, a wider domain upstream from the Hertzian zone and larger particles, representative of metallic contaminants, were considered.

The optical system was focused on the inlet region of the contact to enable direct insight into phenomena occurring upstream of the contact area. The aim of this test was to visualize the entrapment of debris-like particles made of M50 steel and sieved in the range 32–40  $\mu$ m. For this purpose, 1 mg of steel particles was added to the 27 ml of base oil + paint mixture, leading to a low volume fraction of about 0.6%. They were covered by migration–adsorption with fluorescent pigments of the red fire fluorescent paint (as before), which allowed us to follow their motion because of induced fluorescence resulting from the sequential lighting of the contact inlet. The trajectories of the covered steel particles were measurable as long as they remained in the field of view of the microscope. The pulsed lasers allowed us to impose a maximum sequential frequency of 15 Hz ( $T_s = 0.66$  s at the minimum), which in turn enforced a low mean entrainment speed (0.005 m/s in the present work) to perform a Lagrangian-type particle tracking.

Figure 8b presents a series of six photographs that clearly show the entrapment of a single steel particle carried by the lubricant for the conditions  $w = 10$  N and  $U_m = 0.005$  m/s. In the first five photographs, a white dotted circle has been plotted around the steel particle to make it easier to follow its trajectory, before and during its entrapment. Two iso-thickness lines (red dotted lines in Fig. 8b), calculated with an in-house EHD solver [19, 20] applied to the glass–steel contact (see Fig. 8a), were also plotted; they correspond to the minimum and maximum diameters (32  $\mu$ m and 40  $\mu$ m) of the steel particles used in this study. The Hertzian zone is represented with a striped

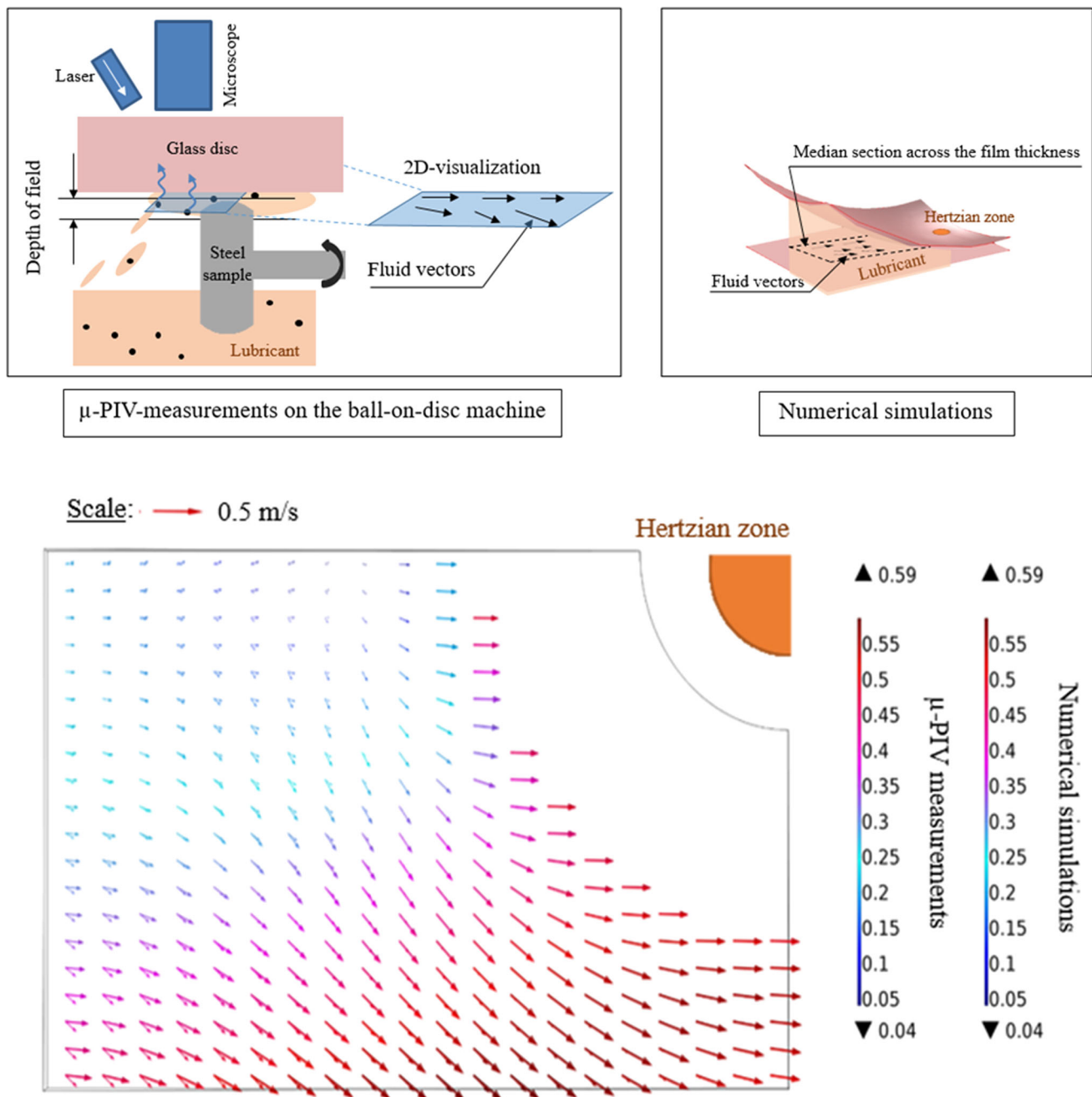


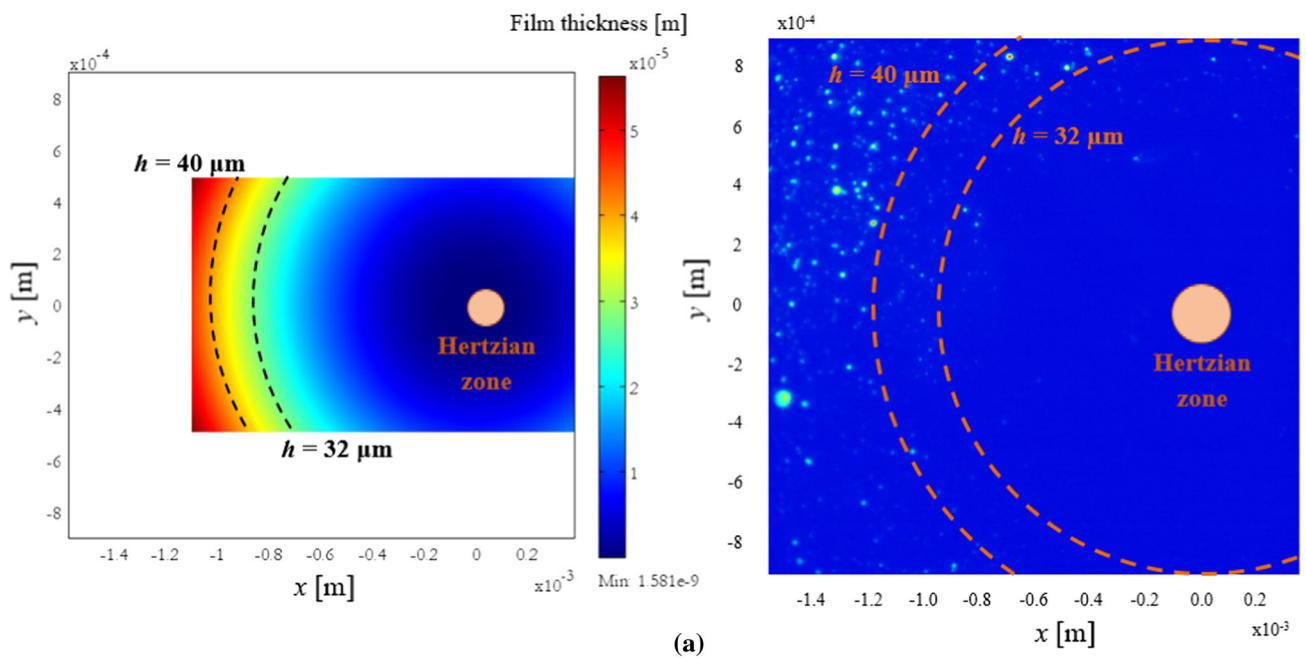
**Fig. 7** Comparison of the velocity vectors distributions obtained from  $\mu$ -PIV and from numerical simulation. Operating conditions:  $U_m = 0.5 \text{ m/s}$ ,  $w = 10 \text{ N}$

disk. There is a clear distinction between the steel and rhodamine particles as the sizes are very different:  $32\text{--}40 \text{ }\mu\text{m}$  for steel particles and  $10 \pm 4 \text{ }\mu\text{m}$  for rhodamine ones (see Fig. 2).

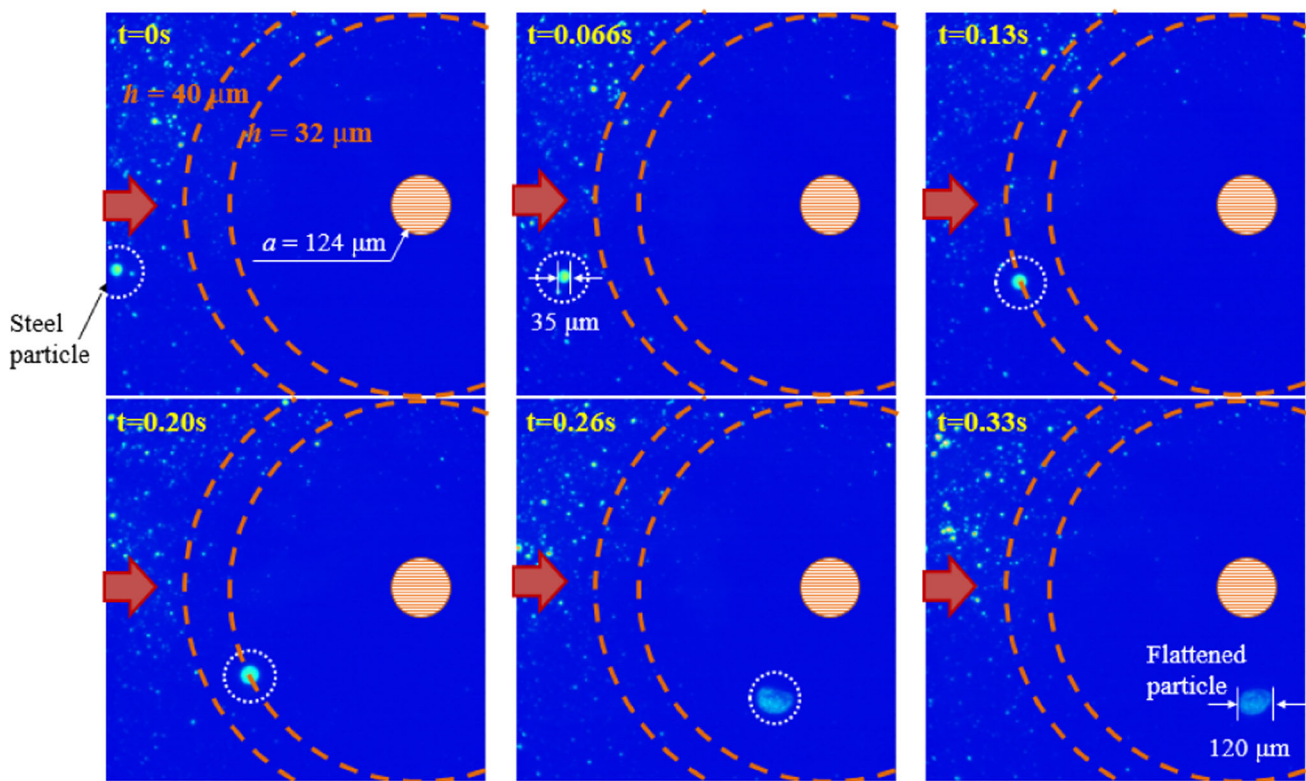
The entrapment process followed different steps. In the first three pictures in Fig. 5b, the (circled) steel particle is carried by the fluid along the velocity direction until it reaches a film thickness close to its diameter, estimated to be  $35 \text{ }\mu\text{m}$ . Once being entrapped, between

0.13 and 0.20 s (the third and fourth photographs), the particle starts moving toward the contact side; the particle also starts to deform, with its diameter changing between two consecutive photographs. Between 0.20 and 0.26 s (the fourth and fifth photographs), the same trends are amplified, in particular the diameter growth. In the two last photographs, the particle moved forward again, entrained by the frictional forces imposed by the contacting surface.





(a)



(b)

**Fig. 8** Online observation of a particle entrapment nearby a steel–glass circular contact ( $U_m = 5$  mm/s;  $w = 10$  N;  $\times 10$  objective; field size of  $1.805 \times 1.820$  mm): (a, left) film thickness distribution

obtained numerically; (a, right) picture of the contact. (b) Series of 6 successive pictures taken between  $t = 0$  s and  $t = 0.33$  s

The debris-like particle tracked in Fig. 8 was made of M50 steel; it was therefore ductile and could deform in the contact, as mentioned by Dwyer-Joyce [23], which was

consistent with the processes of entrapment and deformation described here. Moreover, the final size of the particle appeared to be roughly elliptical, about  $120 \mu\text{m} \times 100 \mu\text{m}$

(length  $\times$  width), which corresponds to an area of  $9425 \mu\text{m}^2$ , assuming that the photographs were taken with appropriate focus and contrast to represent the actual dimensions. The initial particle diameter was  $35 \mu\text{m}$ , leading to a volume of  $22,449 \mu\text{m}^3$ . Hence, the film thickness at the particle at  $t = 0.26 \text{ s}$  ( $400 \mu\text{m}$  off-axis from the Hertzian contact center) should be approximately equal to  $22,449/9425 = 2.4 \mu\text{m}$ . This value was consistent with the numerical prediction of  $2 \mu\text{m}$  for the film gap in the corresponding location.

The fluorescence technique has thus offered a new insight into the trapping of debris-like particles by allowing their tracking well upstream of the Hertzian zone, where they were entrained by the lubricant flow, until their entrapment near the contact area. To the best of our knowledge, this is the first time that such a mechanism has been recorded step by step in situ.

### 3.3 Ellipticity Effect in the Contact Inlet

Particle entrapment in circular point contacts has been rather intensively studied, but in reality, this kind of contact appears only in a limited number of cases. The contacts between rolling elements and rings are generally elliptical. In a previous study [24], the authors highlighted that the contact configuration (i.e., the ellipticity ratio) directly affects the probability of particle entrapment, which was found to be drastically reduced within elliptical contacts compared with circular ones. In [24], numerical simulations confirmed that intense lubricant backflows occur within elliptical contacts, due to stronger hydrodynamic effects. Other studies, such as the work of Hsiao et al. [16], proposed an evaluation of the streamlines in elliptical EHD contacts but without experimental validation.

In this part of the work, the lubricant used was the turbine oil to which rhodamine particles had been added (see Sect. 2). The buoyancy effects could be considered negligible, in agreement with the settling velocity estimation computed from the steady-state expression given by Tropea et al. [25]. Assuming a mean radius of the seeding particles of  $5 \mu\text{m}$  ( $\pm 2 \mu\text{m}$ , see Fig. 2), their settling velocity would be  $0.8 \mu\text{m/s}$ . Given the range of mean entrainment velocities of  $0.005\text{--}3 \text{ m/s}$ , the particles would have no time to settle and the rhodamine fragments could be properly used as tracers of the lubricant motion. The tests were performed on the same ball-on-disk machine as before, but with spherical- and barrel-shaped steel samples, to mimic EHD contacts with  $k$  values of 1, 3.5, and 8, as indicated in Table 2.

To make the motion of fluorescent particles observable, the chosen mean entrainment speed and sequential frequency were the same as in the previous section ( $0.005 \text{ m/s}$  and  $15 \text{ Hz}$ ). This allowed us to observe whether differences

between the circular and elliptical configurations appeared upstream and around the contact areas. As shown in Fig. 9 for a circular contact ( $k = 1$ ), a large amount of lubricant bypassed the contact zone, but the general motion of the lubricant along the center line remained oriented toward the Hertzian contact zone, and no backflow was observed. By contrast, upstream from an elliptical contact, for  $k$  values of either 3.5 or 8, most of the lubricant was clearly subjected to strong backflows (Figs. 10, 11). The particles carried by the lubricant first moved forward, toward the contact area, before being rejected backward. The larger the ellipticity ratio, the stronger the backflows, making it more difficult for the particle to approach the contact area. Therefore, the fluorescence technique combined with particle tracking has allowed us to demonstrate the existence of lubricant backflows within EHD contacts, especially in an elliptical configuration, thus confirming our previous numerical and experimental results [24].

### 3.4 Additional Remarks and Prospect

The extension of a lubricated contact is limited by air–lubricant frontiers located all around. These “frontiers” depend on the operating conditions and thus on the lubrication regime, as postulated by Hamrock and Dowson [26], and have been studied numerically [26–28] as well as experimentally [29, 30]. Particular attention has also been paid to the exit zone, in order to properly characterize the pressure field that exists in the so-called cavitation (or film rupture) area. Bruyere et al. [17] developed a two-phase model able to predict the position and shape of the outlet meniscus in line contacts, for diverse capillary numbers and sliding ratio conditions. It is generally assumed that, downstream from EHD contacts, the lubricant is subjected to such negative pressure gradients that it can be partially vaporized by the so-called cavitation mechanism. In reality, while the lubricant is expelled and stretched at high rate at the contact outlet, it still adheres to the surfaces in thin layers [29, 30], and the so-called cavitation zone is embedded in between them. From the work and results presented so far, a fluorescence-based method appears to be an efficient way to localize the lubricant and determine the menisci positions. Indeed, fluorescent particles are suspended in the lubricant and are consequently visible in the fluid region only, and not in the gaseous domain, as depicted in the right side of Fig. 12. This figure describes the complementarity between two in situ optical techniques applied in the outlet region of a glass–steel EHD contact operated with a normal load of  $10 \text{ N}$  and an entrainment velocity of  $0.5 \text{ m/s}$ . On the left side of Fig. 12, a white light source is used; the white region corresponds to the gaseous phase present at the contact outlet. The contrast in the picture reveals the fingers left by the

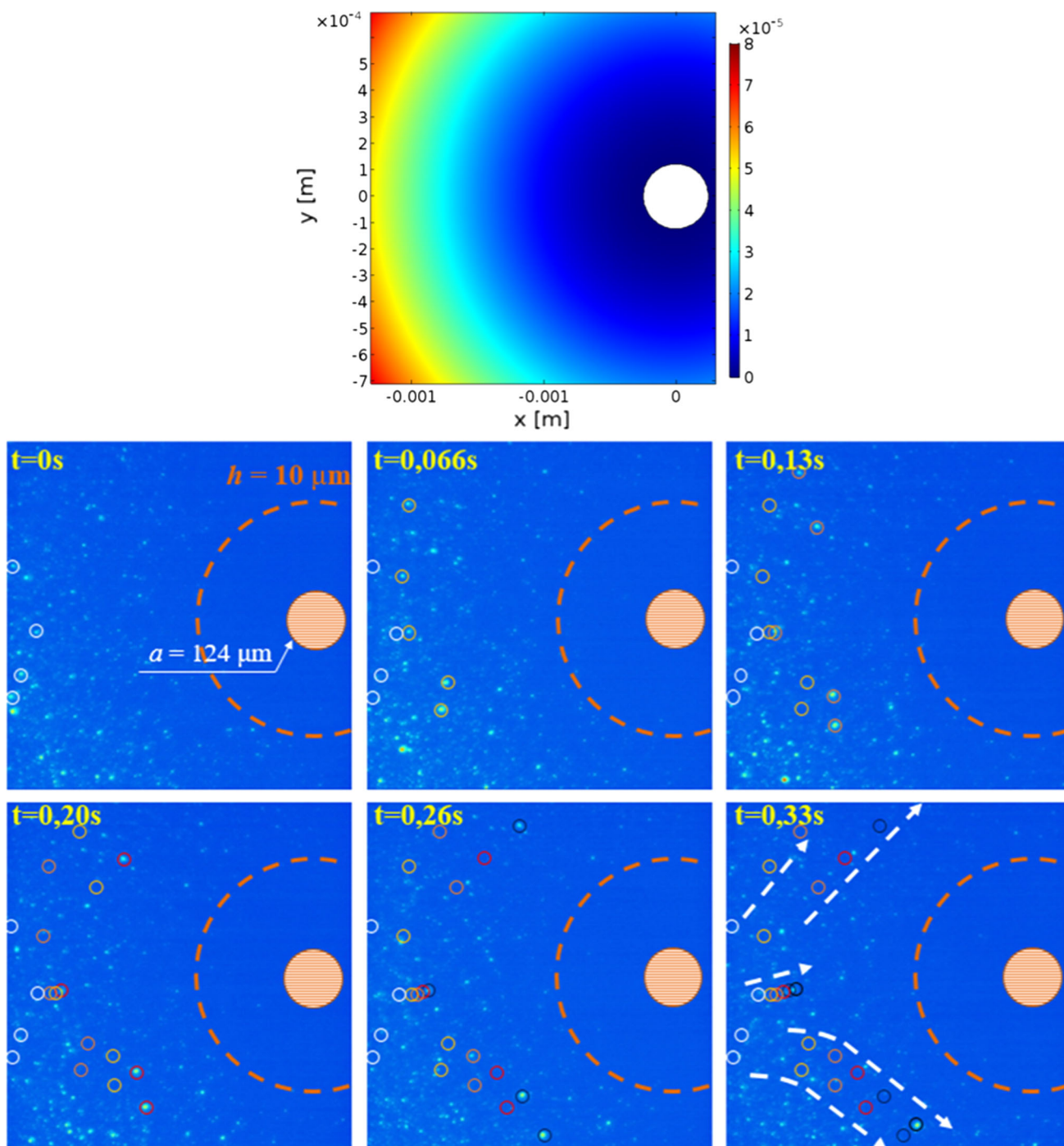


**Fig. 9** Tracking of fluorescent particles upstream a circular contact formed between a steel sphere ( $R_x = R_y = 12.7$  mm) and a glass disk. The particles are excited by a 532-nm laser beam. The *top figure* gives the gap thickness upstream the contact zone. The positions of 4 and then 5 of them identified by *colored circular marks* are tracked versus

time, each *color* being associated with a different time. The previous positions are conserved to better describe the particles motion. Note that 3 particles have left the area of observation (indicated by *arrows* that extend to the edge of the picture). Operating conditions:  $U_m = 0.5$  m/s,  $w = 10$  N (Color figure online)

separation of the ball rolling over the disk surface and gives a first estimation of the distribution of the lubricant still present in that region. On the right side, fluorescence indicates (by the absence of signal in the central zone) that an extremely low volume of lubricant remained on the

contacting surfaces. The addition of fluorescent particles in the lubricant nevertheless helps to capture the gas-liquid frontier at the contact exit, which in this case resembles vertical, wavy walls (underlined by two bright lines in Fig. 12, right).

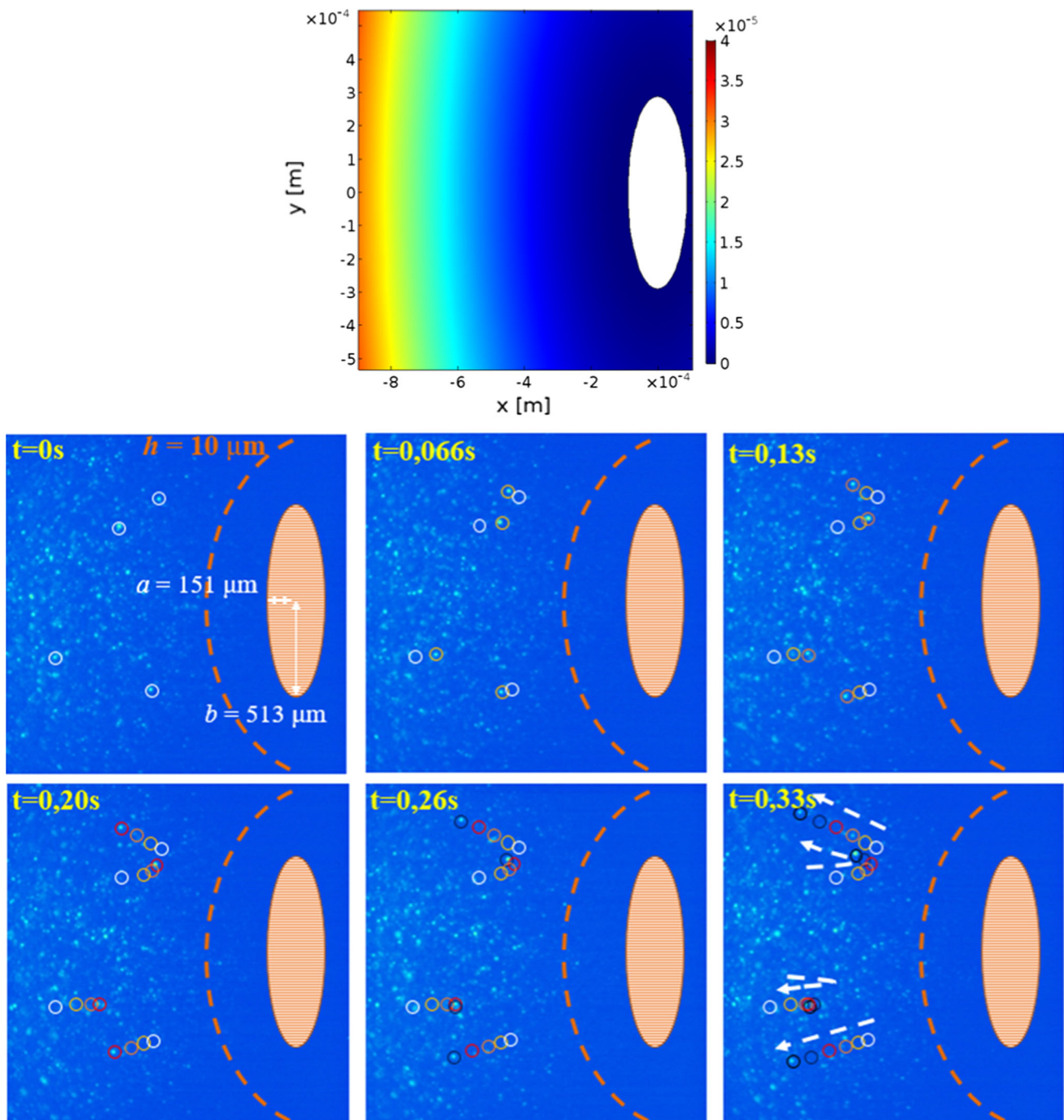


**Fig. 10** Tracking of fluorescent particles upstream an elliptical contact ( $k = 3.4$ ) formed between a steel roller ( $R_x = 13.1$  mm,  $R_y = 84.2$  mm) and a glass disk. The particles are excited by a 532-nm laser beam. The *top figure* gives the gap thickness upstream the contact zone. The positions of 4 of them

identified by *colored circular marks* are tracked versus time, each color being associated with a different time. The previous positions are conserved to better describe the particles motion. Operating conditions:  $U_m = 0.5$  m/s,  $w = 50$  N (Color figure online)

Lubricant replenishment fingers have been widely studied, particularly in the context of grease lubrication, by Cann [31, 32] and more recently by Huang et al. [33], for instance. Here, a new method is suggested for observing the lubricant flow that supplies the

replenishment fingers. This method is illustrated in Fig. 13. The foreground represents a map of the mean velocity field processed from a  $\mu$ -PIV analysis under the same operating conditions as for Fig. 12. A color picture of the same contact and its surroundings, illuminated by

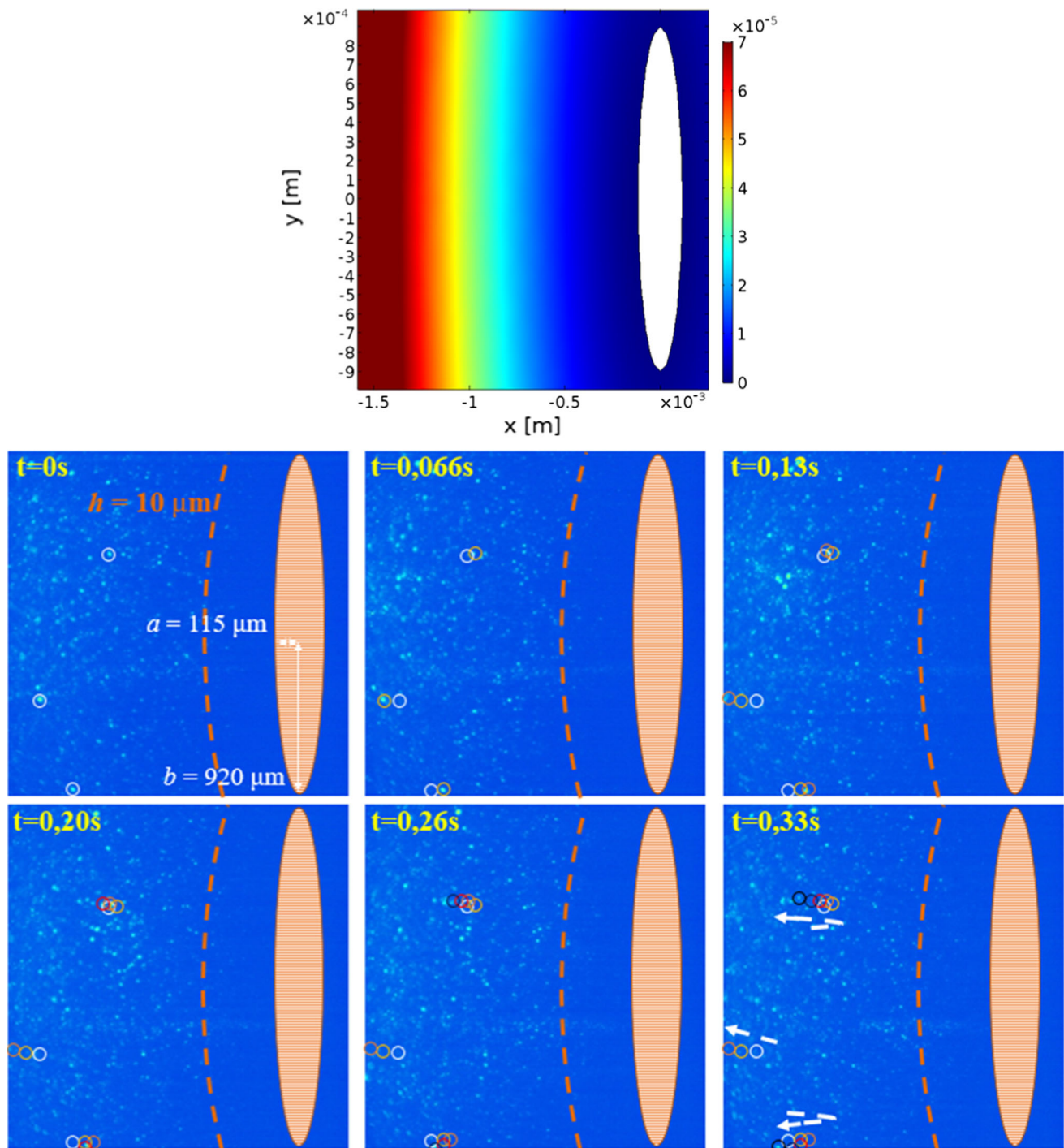


**Fig. 11** Tracking of fluorescent particles upstream an elliptical contact ( $k = 8$ ) formed between a steel roller ( $R_x = 13.1 \text{ mm}$ ,  $R_y = 330 \text{ mm}$ ) and a glass disk. The particles are excited by a 532-nm laser beam. The *top figure* gives the gap thickness upstream the contact zone. The positions of 3 of them

identified by *colored circular marks* are tracked versus time, each *color* being associated with a different time. The previous positions are conserved to better describe the particles motion. Operating conditions:  $U_m = 0.5 \text{ m/s}$ ,  $w = 50 \text{ N}$  (Color figure online)

white light, is superimposed in the background. This technique is applicable for all the operating conditions tested throughout this study, including the elliptical contact configuration. In Fig. 13, the replenishment

lubricant flow is clearly apparent through the velocity vectors. The lubricant that bypasses the contact is then carried toward the outlet zone and is finally entrained toward the replenishment fingers.

**Fig. 12** Visualization of the outlet region of an EHD circular contact by means of white light analysis (*left*) and fluorescent particles (*right*). Operating conditions:  $U_m = 0.5 \text{ m/s}$ ,  $w = 10 \text{ N}$

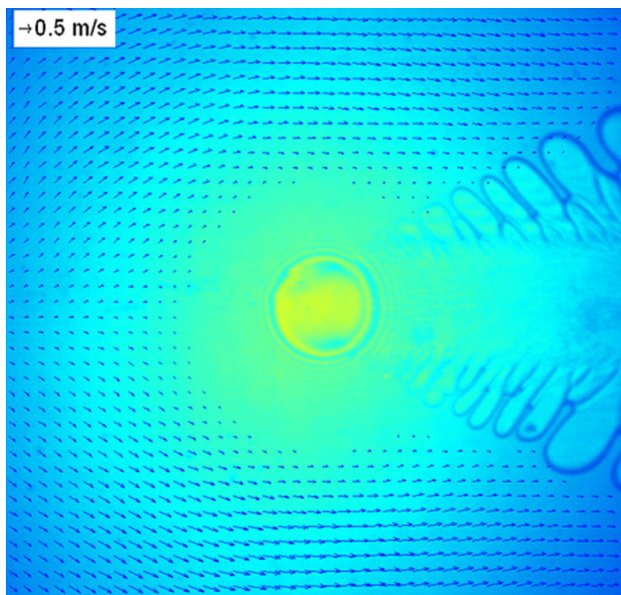
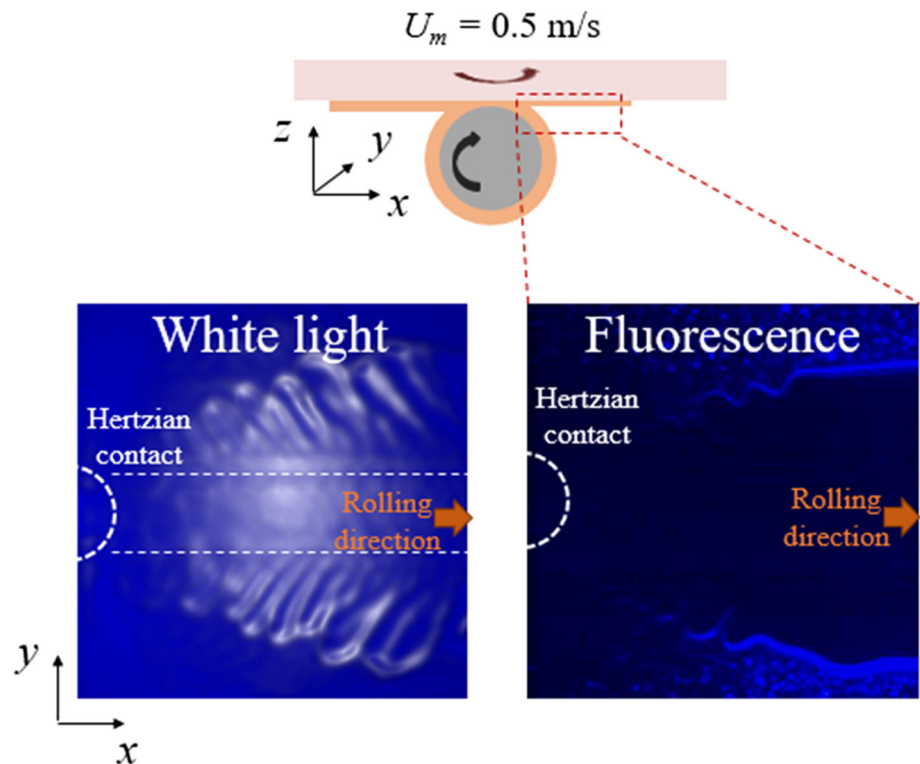


**Fig. 13** Superposition of results from two complementary techniques applied to a circular steel–glass contact ( $U_m = 0.5 \text{ m/s}$ ,  $w = 10$ ). In the foreground, instantaneous velocities field by  $\mu$ -PIV analysis. Background: digital RGB picture of the same contact illuminated by white light

#### 4 Conclusion

The aim of this work was to present an innovative way to analyze EHD contacts and in particular the phenomena leading to contaminant particle entrapment. The

combination of induced fluorescence of selected particles and  $\mu$ -PIV analysis to track specific particle trajectories has allowed the validation of the following statements.

- These fluid mechanics techniques are suitable for tackling EHL-related problems and could be adapted for implementation in classical ball-on-disk tribometers.
- Lubricant behavior can be thoroughly analyzed by the particle tracking method, by simply adding fluorescent dyes to the lubricant. Mapping of the instantaneous velocity vectors brings new in situ and direct insights on the lubricant flow in and around the classical contact area and enables the validation of numerical models.
- The fluorescence technique offers a straightforward way to follow the entrapment of a contaminating steel particle in situ, because of the formation of a fluorescent over-layer. The presence of important backflows in the inlet area of wide elliptical contacts was evidenced experimentally. It was shown that this particular feature prevents the entrapment of contaminant particles.
- This work highlighted the fact that both  $\mu$ -PIV and particle tracking techniques are powerful experimental methods to be further developed in EHL and in the lubrication domain in general. The combination of these techniques offers interesting prospects concerning, for example, the study of replenishment fingers in the outlet of EHD contacts.

**Acknowledgements** This work was carried out at the Laboratoire de Mécanique des Contacts et des Structures (LaMCoS) and was funded by the “Lubricated Interfaces for the Future” research chair established between INSA Lyon and the SKF company. The authors acknowledge Guillermo Morales-Espejel (SKF-ERC) for his technical expertise.

## References

- Albahrani, S.M.B., Philippon, D., Vergne, P., Bluet, J.M.: A review of in situ methodologies for studying elastohydrodynamic lubrication. *Proc. Inst. Mech. Eng. Part J J. Eng. Tribol.* **230**(1), 86–110 (2016)
- Grant, I.: Particle image velocimetry: a review. *Proc. Inst. Mech. Eng. Part C J. Mech. Eng. Sci.* **211**(1), 55–76 (1997)
- Santiago, J.G., Wereley, S.T., Meinhart, C.D., Beebe, D.J., Adrian, R.J.: A particle image velocimetry system for microfluidics. *Exp. Fluids* **25**(4), 316–319 (1998)
- Nogueira, S., Sousa, R.G., Pinto, A., Riethmuller, M.L., Campos, J.: Simultaneous PIV and pulsed shadow technique in slug flow: a solution for optical problems. *Exp. Fluids* **35**(6), 598–609 (2003)
- Bair, S., Qureshi, F., Winer, W.O.: Observations of shear localization in liquid lubricants under pressure. *J. Tribol.* **115**(3), 507–513 (1993)
- Reddyhoff, T., Choo, J.H., Spikes, H.A., Glovnea, R.P.: Lubricant flow in an elastohydrodynamic contact using fluorescence. *Tribol. Lett.* **38**(3), 207–215 (2010)
- Horvat, F.E., Braun, M.J.: Comparative experimental and numerical analysis of flow and pressure fields inside deep and shallow pockets for a hydrostatic bearing. *Tribol. Trans.* **54**(4), 548–567 (2011)
- Li, J.X., Höglund, E., Westerberg, L.G., Green, T.M., Lundström, T.S., Lugt, P.M., Baart, P.:  $\mu$ PIV measurement of grease velocity profiles in channels with two different types of flow restrictions. *Tribol. Int.* **54**, 94–99 (2012)
- Ponjavic, A., Chennaoui, M., Wong, J.S.S.: Through-thickness velocity profile measurements in an elastohydrodynamic contact. *Tribol. Lett.* **50**(2), 261–277 (2013)
- Albahrani, S. M. B.: Photoluminescent CdSe/CdS/ZnS quantum dots for temperature and pressure sensing in elastohydrodynamic contacts. PhD Thesis defended on March 22, 2016 at INSA-Lyon, 2016LYSEI016, Université de Lyon (2016)
- Molimard, J., Query, M., Vergne P.: New tools for the experimental study of EHD and limit lubrications. In: Dowson, D., et al. (ed.) Proceedings of the 25th Leeds-Lyon Symposium on Tribology “Lubrication at the Frontier”. Lyon, 8–11 September 1998. *Tribology Series* 36, pp. 717–726. Elsevier (1999)
- Reiss, P., Chandezon, F.: Nanocristaux semi-conducteurs fluorescents. *Techniques de l’Ingénieur, N M* **2**(030), 1–15 (2004)
- Adrian, R.J.: Particle-imaging techniques for experimental fluid mechanics. *Rev. Fluid Mech.* **23**(1), 261–304 (1991)
- Simoens, S., Ayrault, M.: Concentration flux measurements of a scalar quantity in turbulent flows. *Exp. Fluids* **16**(3), 273–281 (1994)
- Boedec, T., Simoens, S.: Instantaneous and simultaneous planar velocity field measurements of two phases for turbulent mixing of high pressure sprays. *Exp. Fluids* **31**(5), 506–518 (2001)
- Hsiao, H.-S.S., Hamrock, B.J., Tripp, J.H.: Stream functions and streamlines for visualizing and quantifying side flows in EHL of elliptical contacts. *J. Tribol.* **123**(3), 603–607 (2001)
- Bruyere, V., Fillot, N., Morales-Espejel, G.E., Vergne, P.: A two-phase flow approach for the outlet of lubricated line contacts. *J. Tribol.* **134**(4), 041503 (2012)
- Strubel, V., Fillot, N., Ville, F., Cavoret, J., Vergne, P., Mondelin, A., Maheo, Y.: Particle entrapment in hybrid lubricated point contacts. *Tribol. Trans.* **59**(4), 768–779 (2016)
- Habchi, W., Demirci, I., Eyheramendy, D., Morales-Espejel, G.E., Vergne, P.: A finite element approach of thin film lubrication in circular EHD contacts. *Tribol. Int.* **40**(10–12), 1466–1473 (2007)
- Doki-Thonon, T.: Thermal effects in elastohydrodynamic spinning circular contacts. PhD Thesis defended on July, 3 2012 at INSA-Lyon, 2012ISAL0058. INSA de Lyon (2012)
- Cann, P. M., Sayles, R. S., Spikes, H. A., Ioannides, E., Hamer, J. C.: Direct observation of particle entry and deformation in a rolling EHD contact. In: Dowson, D., et al. (ed.) Proceedings of 22nd Leeds-Lyon Symposium on Tribology “The Third Body Concept: Interpretation of Tribological Phenomena”. Lyon, 5–8 September 1995. *Tribology Series* 31, pp. 127–134. Elsevier (1996)
- Chinas-Castillo, F., Spikes, H. A.: Behaviour of colloiddally-dispersed solid particles in very thin film lubricated contacts. In: Dowson, D. et al. (ed.) Proceedings of the 26th Leeds-Lyon Symposium on Tribology “Thinning Films and Tribological Interfaces”. The University of Leeds, 14–17 September 1999. *Tribology Series* 38, pp. 719–731. Elsevier (2000)
- Dwyer-Joyce, R.S.: The life cycle of a debris particle. In: Dowson, D. et al. (ed.) Proceedings of the 31st Leeds-Lyon Symposium on Tribology “Life Cycle Tribology”. The University of Leeds, 7–10 September 2004. *Tribology and Interface Engineering Series* 48, pp. 681–690. Elsevier (2005)
- Strubel, V., Fillot, N., Ville, F., Cavoret, J., Vergne, P., Mondelin, A., Maheo, Y.: Particle entrapment in rolling element bearings: the effect of ellipticity, nature of materials and sliding. *Tribol. Trans.* **60**(2), 373–382 (2017)
- Tropea, C., Yarin, A.L., Foss, J.F.: *Springer Handbook of Experimental Fluid Mechanics*. Springer, Berlin (2007). ISBN 978-3-540-25141-5
- Hamrock, B.J., Dowson, D.: Isothermal elastohydrodynamic lubrication of point contacts: part III—fully flooded results. *J. Lubr. Technol.* **99**(2), 264–275 (1977)
- Chevalier, F., Lubrecht, A.A., Cann, P.M.E., Colin, F., Dalmaz, G.: Starvation phenomena in EHL point contacts: influence of inlet flow distribution. In: Dowson, D. et al. (ed.) Proceedings of 22nd Leeds-Lyon Symposium on Tribology “The Third Body Concept: Interpretation of Tribological Phenomena”. Lyon, 5–8 September 1995. *Tribology Series* 31, pp. 213–223 (1996)
- Damiens, B., Venner, C.H., Cann, P.M.E., Lubrecht, A.A.: Starved lubrication of elliptical EHD contacts. *J. Tribol.* **126**(1), 105–111 (2004)
- Svoboda, P., Kostal, D., Krupka, I., Hartl, M.: Experimental study of starved EHL contacts based on thickness of oil layer in the contact inlet. *Tribol. Int.* **67**, 140–145 (2013)
- Kostal, D., Necas, D., Sperka, P., Svoboda, P., Krupka, I., Hartl, M.: Lubricant rupture ratio at elastohydrodynamically lubricated contact outlet. *Tribol. Lett.* **59**(3), 1–9 (2015)
- Cann, P.M.E.: Starvation and reflow in a grease-lubricated elastohydrodynamic contact. *Tribol. Trans.* **39**(3), 698–704 (1996)
- Cann, P.M.E.: Thin-film grease lubrication. *Proc. Inst. Mech. Eng. Part J J. Eng. Tribol.* **213**(5), 405–416 (1999)
- Huang, L., Guo, D., Wen, S., Wan, G.T.Y.: Effects of slide/roll ratio on the behaviours of grease reservoir and film thickness of point contact. *Tribol. Lett.* **54**(3), 263–271 (2014)